ADVANCED ENERGY MATERIALS
www.advenergymat.de

Macroscopic Displacement Reaction of Copper Sulfide in Lithium Solid-State Batteries

Aggunda L. Santhosha, Nazia Nazer, Raimund Koerver, Simon Randau, Felix H. Richter, Dominik A. Weber, Joern Kulisch, Torben Adermann, Jürgen Janek, and Philipp Adelhelm**

Copper sulfide (CuS) is an attractive electrode material for batteries, thanks to its intrinsic mixed conductivity, ductility and high theoretical specific capacity of 560 mAh g^{-1}. Here, CuS is studied as cathode material in lithium solid-state batteries with an areal loading of 8.9 mg cm^{-2} that theoretically corresponds to 4.9 mAh cm^{-2}. The configuration of the cell is Li | Li_3PS_4 | [CuS (70 wt%) + Li_3PS_4 (30 wt%)]. No conductive additive is used. CuS undergoes a displacement reaction with lithium, leading to macroscopic phase separation between the discharge products Cu and Li_2S. In particular, Cu forms a network of micrometer-sized, well-crystallized particles that seems to percolate through the electrode. The formed copper is visible to the naked eye. The initial specific discharge capacity at 0.1 C is 498 mAh $g(CuS)^{-1}$, i.e., 84% of its theoretical value. The initial Coulomb efficiency (ICE) reaches 95%, which is higher compared to standard carbonate-based liquid electrolytes for the same cell chemistry (≈70%). After 100 cycles, the specific capacity reaches 310 mAh $g(CuS)^{-1}$. With the current composition, the cell provides 58.2 Wh kg^{-1} at a power density of 7 W kg^{-1}, which is superior compared to other transition metal sulfide cathodes.

1. Introduction

Lithium solid-state batteries (SSBs) are studied intensively as potential alternative to conventional lithium-ion batteries (LIBs). In SSBs, the flammable liquid organic electrolyte of LIBs is replaced by a solid electrolyte (SE). Better safety and higher energy densities are the main promises of this approach, yet the practical viability still needs to be proven. The SSB concept also requires different methods for preparing electrodes and cells that are typically compacted at high pressure to achieve a sufficiently high density and close contact between electrode and electrolyte particles. The progress in research and development on SSBs is frequently summarized in literature.[1]

Next to polymer electrolytes,[2] inorganic Li-ion SEs have been developed in recent years.[3] Thiophosphates, garnets, or argyrodites are the most promising inorganic materials classes, each having particular advantages and disadvantages. Despite the considerable improvement in Li^+ conductivity (some structures exhibit a higher conductivity than liquid electrolytes) the limited electrochemical stability window of SEs often leads to side reactions with low potential negative and high potential positive materials.[4] For this reason, in research studies the lithium negative electrode is often replaced by an In–Li alloy as this alloy provides a more stable interface with many SEs and prevents dendrite formation.[5] The use of Li as negative electrode in SSBs, however, remains an important goal as this is one of the few options to significantly increase the specific energy (Wh kg^{-1}) and energy density (Wh L^{-1}) of the cell. Considering positive electrode materials, the large family of layered oxides is mostly studied as their overall superior behavior is well-known from LIBs. However, also conversion-type materials such as TiS_2,[6] CoS,[7] FeS_2,[8] MoS_2, [9] and NiS[10] are studied due to their much higher specific capacity.

An important aspect of SSBs is the preparation of dense cathode composite structures containing SE, active material and, where needed, additives. Close contact between the phases and a suitable 3D structure is required to minimize the

A. L. Santhosha, Dr. N. Nazer, Prof. P. Adelhelm
Department of Chemistry
Humboldt-University of Berlin
Brook-Taylor-Strasse 2, Berlin 12489, Germany
E-mail: philipp.adelhelm@hu-berlin.de

The ORCID identification number(s) for the author(s) of this article can be found under https://doi.org/10.1002/aenm.202002394.

DOI: 10.1002/aenm.202002394

Dr. R. Koerver, S. Randau, Dr. F. H. Richter, Dr. D. A. Weber, Prof. J. Janek
Institute of Physical Chemistry
Center for Materials Research
Justus-Liebig-University Giessen
Heinrich-Buff-Ring 17, Giessen 35392, Germany
E-mail: juergen.janek@uni-giessen.de
Dr. J. Kulisch, Dr. T. Adermann
BASF SE
Ludwigshafen 67056, Germany

Table 1. Properties of the stoichiometric conversion reaction of CuS with lithium at 25 °C, data obtained using HSC chemistry software database.

Cell reaction	Copper sulfide
$2{\cdot}Li + CuS \xrightarrow{\text{discharge}} Cu + Li_2S$	
$\Delta_r G°$ [kJ mol^{-1}]	−379
Number of transferred electrons	2
Voltage vs. Li$^+$/Li [V]	1.96
q_{th} (CuS) by volume [mAh cm^{-3}]	2669
q_{th} (CuS) by weight [mAh g^{-1}]	561
Volume expansion CuS electrode [%]	75
Volume expansion of cell[a)] [%]	−25
Specific energy[a)] [Wh kg^{-1}]	961
Energy density[b)] [Wh L^{-1}]	2283
Conductivity (CuS) [S cm^{-1}]	870 [20]
Mohs hardness of CuS/–	1–1.5[22]

[a)]Assuming the cell reaction; [b)]Charged state.

charge transfer resistance over the phase boundaries and to provide sufficient electronic and ionic conductivity throughout the electrode.[1c,11] A challenge is to maintain this close contact during cycling. Loss of contact might easily occur due to the volume changes of the active material during lithiation/delithiation.[12] This can be counteracted to some extent by applying external pressure.[13] Considering the above, combining soft SEs and soft active materials seems advantageous as their mixtures can be easily densified and contact losses during cycling might be minimized.[10]

Here, we discuss the use of CuS as electrode material for SSBs. Relevant properties of CuS and characteristics of the reaction with lithium at room temperature are summarized in **Table 1**. The idealized reaction is a conversion-type reaction

$$2{\cdot}Li + CuS \underset{\text{charge}}{\overset{\text{discharge}}{\rightleftharpoons}} Cu + Li_2S \quad (1)$$

or generalized for 1:1 binary oxides and sulfides

$$2{\cdot}Li + MeX \underset{\text{charge}}{\overset{\text{discharge}}{\rightleftharpoons}} Me + Li_2X \quad (2)$$

with Me being mostly a 3d transition metal and *X* representing the group 16 elements O and S. It is of note, however, that the Cu–S phase diagram is very complex, containing many off-stoichiometric, intermediate compounds such as $Cu_{2-x}S$ or $Cu_{1.96}S$, meaning that the electrode reaction becomes more complex.[14] A characteristic feature of conversion reactions (Equation 2) is that the initial lithiation leads to the formation of a nanoscopic microstructure containing metal nanoparticles (few nm in size) dispersed in a disordered Li_2X matrix.[15] For example, Cu nanoparticles in the range of 2–3 nm form during the conversion reaction of lithium with CuO.[16] The complex reaction mechanisms combined with large structural changes lead to redox potentials deviating from the expected values. The same behavior is found in case of sodium.[17] The formation of metal nanoparticles is also believed to catalyze the decomposition of liquid electrolytes which contributes to the generally very low initial Coulomb efficiency (ICE) observed for these cell reactions, for example studies on CuO.[18]

The conversion reaction of CuS with Li, however, behaves markedly different. Débart et al. showed (in cells with liquid electrolyte) that instead of forming a nanoscopic structure, lithiation of CuS leads to a macroscopic phase separation.[19] During lithiation, Cu is extruded from the Li_xCu_2S intermediate to form large crystals. This was attributed to the structural similarity between the Li_xCu_2S intermediate phase and Li_2S. Hence, the authors described the reaction as a displacement reaction. Poor rechargeability, however, was identified as a major bottleneck. This issue can be solved by using an ether-based electrolyte as shown by Jache et al.[20] For example, Cu_2S shows a specific capacity of 200 mAh g^{-1} over 150 cycles using 1 M LiTFSI in DOL/DME as electrolyte and the voltage hysteresis is as small at 150 mV at 0.1 C.

Interestingly, copper sulfides have also been used as additive for sulfur cathodes in SSBs to improve the rechargeability (Table S1, Supporting information). A In-Li alloy counter electrode as used in most of these studies is not ideal and can complicate analysis of the voltage profiles.[5,21]

Lastly, it is worth pointing out some more specific properties of CuS that are relevant considering its use in a solid-state device.

- *Conductivity*: An important advantage of copper sulfides is their high overall conductivity reaching 870 S cm^{-1} (CuS) and 70 S cm^{-1} (Cu_2S), for example.[20] These, for ionic compounds very high values are largely due to electronic conductivity. Studies on $Cu_{2-x}S$ with varying stoichiometry showed that the Cu/S ratio strongly influences the ionic (Cu^+) conductivity while the impact on the electronic conductivity is quite small. An activation energy for ion hopping in $Cu_{2-x}S$ of 0.24 eV has been determined by Okamoto and Kawai from which a room temperature partial ionic conductivity of σ(Cu+) = 0.012 S cm^{-1} can be estimated.[23] This is a very high value for ion conduction at room temperature (especially considering other ion conductors of interest for electrochemical devices, e.g. Li-ion or Na-ion conductors). The high electronic conductivity may also eliminate the need for carbon conductive additives.
- *Voltage, specific energy*: The cell voltage after Equation 1 equals 1.96 V which is low compared to many layered oxides and hence a drawback. On the other hand, the specific energy of 961 Wh kg^{-1} for the stoichiometric cell reaction is still quite attractive due to the high specific charge q_{th}(CuS) = 561 mAh g^{-1}. At the same time, using positive electrode materials with low redox potential could alleviate the issue of oxidative sulfide SE decomposition that is known for high potential oxides.[24]
- *Ductility, volume expansion*: An immediate concern of Equation (1) is the large volume expansion of +74% from which one would expect poor cycle life in solid-state devices. This might be alleviated by the high ductility of copper sulfides (Mohs hardness of 1–1.5), especially when combined with soft sulfide electrolytes such as Li_3PS_4.[21a,b]
- *Synthesis*: The mixed (e^-, Cu^+) conducting properties of copper sulfides eases the synthesis. Compared to oxides, which require high calcination temperatures typically between 500 and 1000 °C, copper sulfides form from the elements already at much lower temperature (even at room

temperature).[20] When synthesized, this could be an important benefit related to its CO_2 footprint. Moreover, copper sulfides are naturally occuring minerals.

In view of these advantages, CuS is a very appealing test case for the use of conversion reactions in lithium SSBs. Here, we report on the behavior of CuS in Li-SSBs using Li_3PS_4 as SE (Li|Li_3PS_4|[CuS(70 wt%) + Li_3PS_4(30 wt%)]). Cells with a CuS areal loading of 8.9 mg cm^{-2}, corresponding to a theoretical areal capacity of 4.9 mAh cm^{-2}, are studied. Voltage profiles, ICE, cycle life, and rate capability are discussed. The reaction mechanism is followed by scanning electron microscopy (SEM), EDS, and X-ray photoelectron spectroscopy (XPS) and reveals the unequivocal proof that CuS undergoes a displacement reaction.

2. Results and Discussion

2.1. Synthesis and Structural Characterization of CuS

The CuS active electrode material was produced by solid-state synthesis. Figure S2 (Supporting Information) shows powder X-ray diffraction (XRD) patterns that were obtained by mechanical milling of Cu and S followed by annealing at temperatures of 100 °C, 200 °C, and 300 °C for 3h. The diffraction pattern of the sample treated at 300 °C (**Figure 1**A) confirms the hexagonal covellite phase of CuS with space group *P63/mmc* and the lattice constants are a = 0.3792 nm, b = 0.3972 nm, and c = 1.6344 nm (JCPDS file number 06-0464). The SEM images in Figure 1B show that the material consists of irregularly shaped agglomerates in the nanometer and micrometer range. The thermal stability of CuS under oxygen atmosphere was studied by thermogravimetric analysis (TGA) (Figure S3, Supporting Information). CuS is stable up to around 270 °C. A minor weight loss due to decomposition is followed by $CuSO_4$ formation,[25] which is the thermodynamically preferred product.

2.2. Electrochemical Performance of Solid-State Li/CuS Cells

Solid-state cells were assembled based on the materials sequence Li|Li_3PS_4|[CuS 70 wt% + Li_3PS_4 (30 wt%)]. The Li_3PS_4 SE was provided by BASF SE and showed an ionic conductivity of 1.5 × 10^{-4} S cm^{-1} at 25 °C and an activation energy of 0.3 eV (Figure S4B, Supporting Information). **Figure 2**A shows the galvanostatic charge–discharge voltage profiles between 0.7 and 3.0 V of the 1st, 5th, 50th, and 100th cycle. The current density at 0.1 C was 0.49 mA cm^{-2} (56 mA g^{-1}). Note that 1 C equals 560 mA g^{-1} according to the theoretical specific capacity of CuS. The cell delivers initial specific discharge and charge capacities of 498 and 474 mAh g^{-1}, respectively, or 349 and 332 mAh g^{-1} including the weight of the SE in the cathode. Note that all the capacity values in this work refer to the total mass of CuS unless stated otherwise. The ICE reaches 95%, which is significantly higher compared to the same reaction in cells with common liquid carbonate-based electrolytes (ICE ≈ 70%) and even ether-based electrolytes (≈90%).[20] Note that ICE values also can depend on the exact cycling protocol,[26] however, results for the studies mentioned here were all obtained with galvanostatic measurements. The voltage profile is similar to the previously

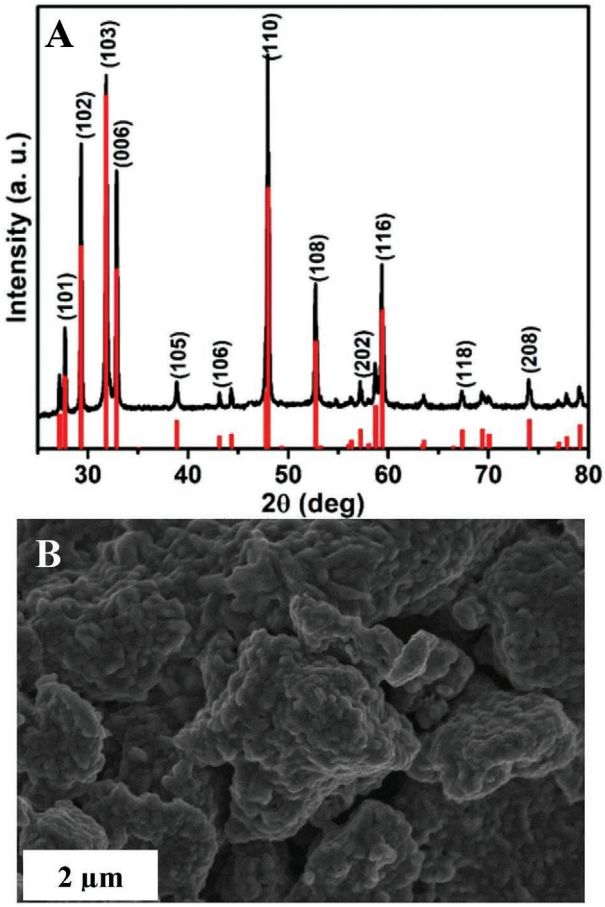

Figure 1. CuS synthesized at 300 °C (3h) A) XRD pattern and comparison with standard JCPDS file number 06-0464. B) Scanning electron microscopy (SEM) images.

reported works of CuS in liquid electrolyte [24c,27]. The two distinct discharge plateaus appear at 2.1 and 1.7 V suggesting that the electrochemical reaction pathway proceeds in two steps; where, the high voltage (2.1 V) plateau is linked to the formation of Cu_2S with various stoichiometries (Equation 3) and the low voltage (1.7 V) plateau is associated with the displacement reaction to form copper and Li_2S (Equation 4).

$$CuS + Li \rightarrow 0.5Li_2S + 0.5Cu_2S \quad \text{at 2.1 V} \quad \Delta_r G° = -206.85 \text{ kJ mol}^{-1} \tag{3}$$

$$0.5Cu_2S + Li \rightarrow Cu + 0.5Li_2S \quad \text{at 1.7 V} \quad \Delta_r G° = -171.97 \text{ kJ mol}^{-1} \tag{4}$$

During charging, two plateaus can be observed at 1.80 and 2.25 V indicating that the reaction is reversed. This is different from cells with liquid electrolyte that show several small potential steps followed by one long flat plateau during charging.[20]

In a recent systematic work from Hosseini et al. on CuS/sulfur/carbon/SE electrodes, the CuS/SE electrode cycled in a solid-state cell with LiIn as anode and LiI–Li_3PS_4 as SE showed a specific capacity significantly exceeding the theoretical value of CuS during charging and cycling.[28] This increased capacity is due to redox activity of the LiI–Li_3PS_4 SE when being

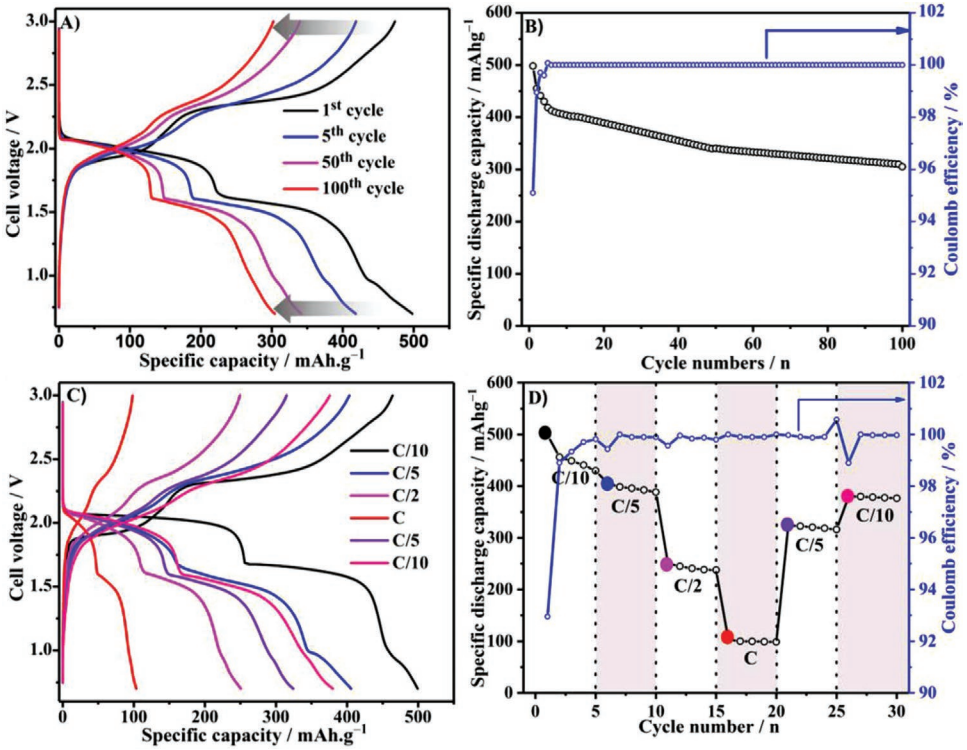

Figure 2. Electrochemical properties of the Li/CuS solid-state cell. A) Galvanostatic charge–discharge profile for 1st, 5th, 50th, and 100th cycles at a constant current density of 0.1 C in the voltage range of 0.7 to 3.0 V. B) Specific discharge capacity and Coulomb efficiency at 0.1 C over cycling. C) Voltage profiles at different current densities (0.1, 0.2, 0.5, and 1 C, 1 C = 560 mAh g^{-1}). D) Specific discharge capacity and Coulomb efficiency at different current densities.

ball-milled during electrode preparation.[29] At this point, it is important to note that Hosseini et al. used ball milling (with 50 wt% SE) for preparing the composite electrode whereas we used hand grinding. To estimate the contribution of Li_3PS_4 to the capacity in our experiment, the cells Li|Li_3PS_4||[Li_3PS_4(90 wt%) + Graphite(10 wt%)] and Li|Li_3PS_4|Li_3PS_4(30 wt%) + Copper (70 wt%) were assembled (Figure S5A,B, Supporting Information). Only negligible activity was observed, i.e., the reported capacity in our study is by and large due to CuS (and not due to Li_3PS_4). Hand grinding therefore seems to minimize the effect of obtaining excess capacity due to the SE.

The stability of the SE in contact with lithium was tested in symmetric cells (Li|Li_3PS_4|Li) which showed sufficient stability over 200 h of plating/stripping (Figure S6, Supporting Information). Long-term rechargeability of the CuS of the electrode was tested by galvanostatic cycling. Figure 2a shows the charge–discharge profile of 1st, 5th, 50th, and 100th cycles at a current of 0.1 C (560 mA g^{-1}). Although capacity fading occurs, the cell could be cycled over 100 cycles reaching 305 mAh g^{-1} at the end. This corresponds to an average specific capacity loss of 1.1 mAh g^{-1} per cycle. Several mechanisms can contribute to the capacity loss of batteries over cycling (ageing) that are hard to deconvolute.[30] In the present case, we could not obtain more detailed information on the cell ageing, however, likely causes of capacity fade are contact losses as a result of the large volume changes of the active material as well as grain coarsening of the poorly conductive Li_2S discharge product.

The rate performance was evaluated by varying the current rate from 0.1 to 1 C with five-cycle intervals (1 C equals 560 mA g^{-1}). Specific discharge capacities and selected voltage profiles are shown in **Figure 3**C,D. The initial cycle (cycle 1) at 0.1 C showed discharge–charge capacities of 499 and 463 mAh g^{-1}, respectively, corresponding to an ICE of 92%. Higher currents lead to lower specific capacity values with 405 mAh g^{-1} (cycle 6, 0.2 C), 250 mAh g^{-1} (cycle 11, 0.5 C), and 103 mAh g^{-1} (cycle 16, 1 C), respectively. The expected lower capacity is due to increasing polarization as can be seen from the voltage profiles. Subsequent lowering of the C-rate leads to an increase in capacity. While the initial specific capacity could not be obtained, the cell still delivered 324 mAh g^{-1} (cycle 21, 0.2 C) and 380 mAh g^{-1} (cycle 26, 0.1 C). The capacity loss over 30 cycles is well in line with the results shown in Figure 3B.

2.3. Ex Situ Study of the Solid-State CuS Electrode

In order to study the electrode reaction in more detail, the composite electrodes (CuS + SE) were analyzed before cycling, after discharge and after charging by SEM, EDX, XRD, and XPS.

2.3.1. SEM, EDX, XRD Studies

Figure 4 shows the SEM image of the pristine electrode and corresponding EDX maps for Cu, S, and P. Both electrode components can be clearly distinguished on the micrometer range, which is a result of the relatively mild hand grinding during electrode preparation. Although the CuS particles show some aggregation, they are well embedded in the SE phase.

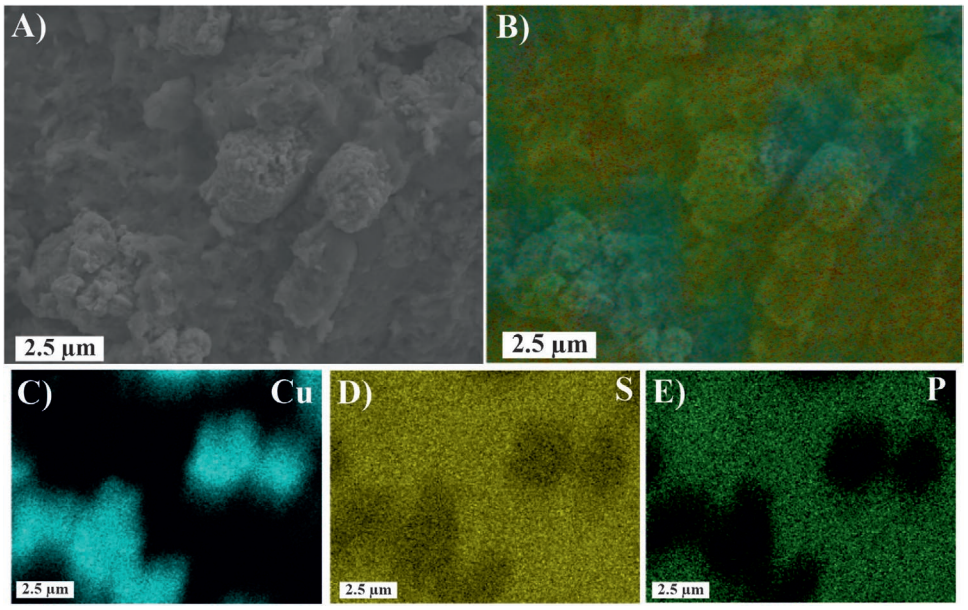

Figure 3. Top view scanning electron microscopy (SEM) image A) and EDX overlay B) of the cathode composite (CuS + Li_3PS_4) before discharging. C–E) EDX elemental mapping of Cu, S, and P.

The most relevant finding of the study is seen in Figure 4, which shows SEM and EDX results of the electrode after the 1st discharge to 0.7 V at 0.1 C. Compared to the pristine cathode, the image in Figure 4a shows that lithiation leads to significant changes in the electrode morphology in the micrometer range. Large, micrometer-sized Cu crystals are visible that seem to form a continuous network throughout the electrode. The formation of large copper crystals as a result of a displacement reaction between the Cu_2S intermediate and Li (Equation 4) has been observed by TEM by Débart et al. and has been explained with a similarity in crystal structures between Cu_2S and Li_2S.[19] In their study, a liquid electrolyte was used which means that the electrode could freely expand. Here, we find that the same mechanism occurs in the solid-state despite the confinement of the all-solid-state configuration. Moreover, the crystallites appear to be much larger in the solid-state cell with copper being even visible by eye (Figure S7, Supporting Information). The respective EDX mappings of Cu, P, and S are also shown in Figure 4.

The displacement reaction was confirmed by ex situ XRD (Figure S8A, Supporting Information) of the same electrode, which shows clear reflections of Cu. As shown in Table 1, the formation of Cu and Li_2S during discharge theoretically leads to

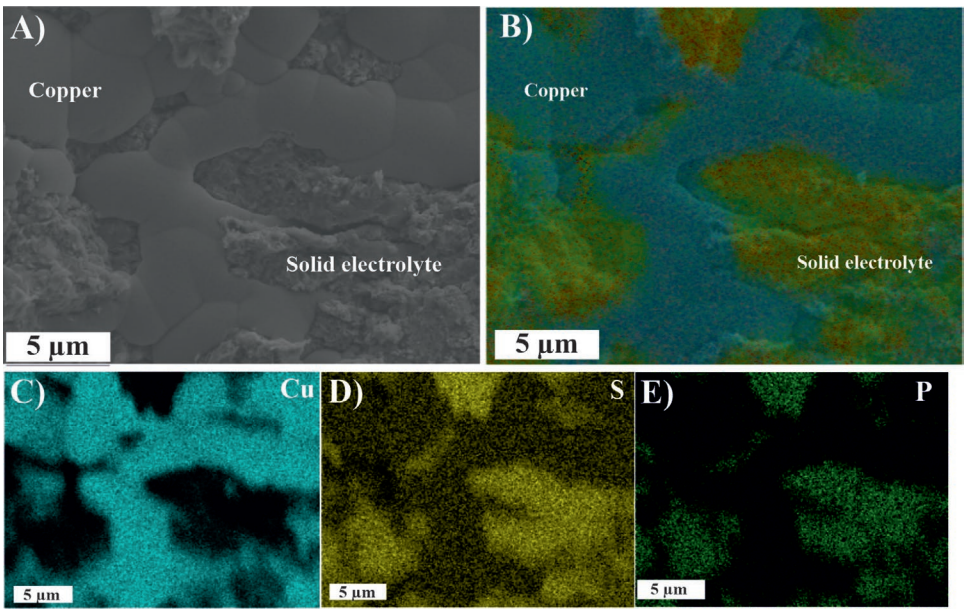

Figure 4. Top view scanning electron microscopy (SEM) image A) and EDX overlay B) of the cathode composite after discharge. C–E) EDX elemental mappings of Cu, S, and P, respectively.

a volume expansion of the cathode active material by 75%, i.e., the electrode should possess sufficient porosity. On the other hand, based on the anode and cathode, discharging leads to volume shrinkage (–25%). It is generally difficult to determine the exact porosity of the cathode in the SSB cell however, we did not observe larger voids by SEM.

SEM/EDX images after charging are shown in Figure S9 (Supporting Information). The well-defined crystallinity of the copper particles has vanished. In accordance, also the Cu reflections in the XRD patterns (Figure S8B, Supporting Information) disappeared. EDX mapping shows an overlap of Cu and S signals indicating that copper was re-oxidized during charging to form copper sulfide. We were not able to identify the type of copper sulfide (CuS, Cu_2S, $Cu_{2-x}S$, and so forth). The XRD results suggest that largely amorphous products are formed during charging. However, the high ICE value of around 95% (Section 2.2) indicates that the reaction is nearly reversed upon charging. It is of note that we never observed larger cracks by SEM, neither after discharging or charging. This is quite intriguing considering the large volume expansion of the reaction and the displacement mechanism that leads to phase separation on the micrometer range. Overall, this means that the complete electrode undergoes ductile deformation during cycling.

2.3.2. XPS Studies

XPS was applied to study the chemical states of the ($CuS + Li_3PS_4$) electrode before and after discharge. **Figure 5**A,B shows the depth profile plots of the S 2p spectra with etching times of 0, 10, 30, and 50 min. In all cases, the spectra are dominated by signal from the SE related to S $2p_{3/2}$ and S $2p_{1/2}$ at binding energies (BE) of 161.5 and 162.6 eV (both purple), respectively. The S $2P_{3/2}$ major component is due to nonbridging sulfur bond S (P–S–Li) of the PS_4^{3-} tetrahedra unit structure[31] and the S $2P_{1/2}$ minor component is associated with bridging S (P–S–P) of the $P_2S_7^{4-}$ ditetrahedra units. Before discharge, the weaker signal at 160.5 eV (red) corresponds to S^{2-}, which indicates the presence of copper sulfide. Etching leads to a slight change in peak intensities but the results after 10, 30, and 50 min are very similar. After discharge, one can clearly see an increasing intensity of the peak at 160.5 eV (red) due to Li_2S (Li-S-Li), which is the expected discharge product (along with Cu).[24b,c,32]

From the above results, the reaction involving the formation of large Cu crystals and Li_2S is schematically illustrated in **Figure 6**. As mentioned above, the displacement mechanism is unique for the reaction of CuS with Li and surprising considering the solid-state cell approach. Other conversion reactions lead to the formation of a nanoscopic structure with metal nanoparticles and require larger amounts of conductive additive. The illustration also includes information on the composition of the electrode with the content of the active material being 70 wt% or 48 vol%. No conductive additive was used.

2.4. Benchmarking

The results of this study are summarized in a Ragone plot together with selected publications of comparable SSBs, which

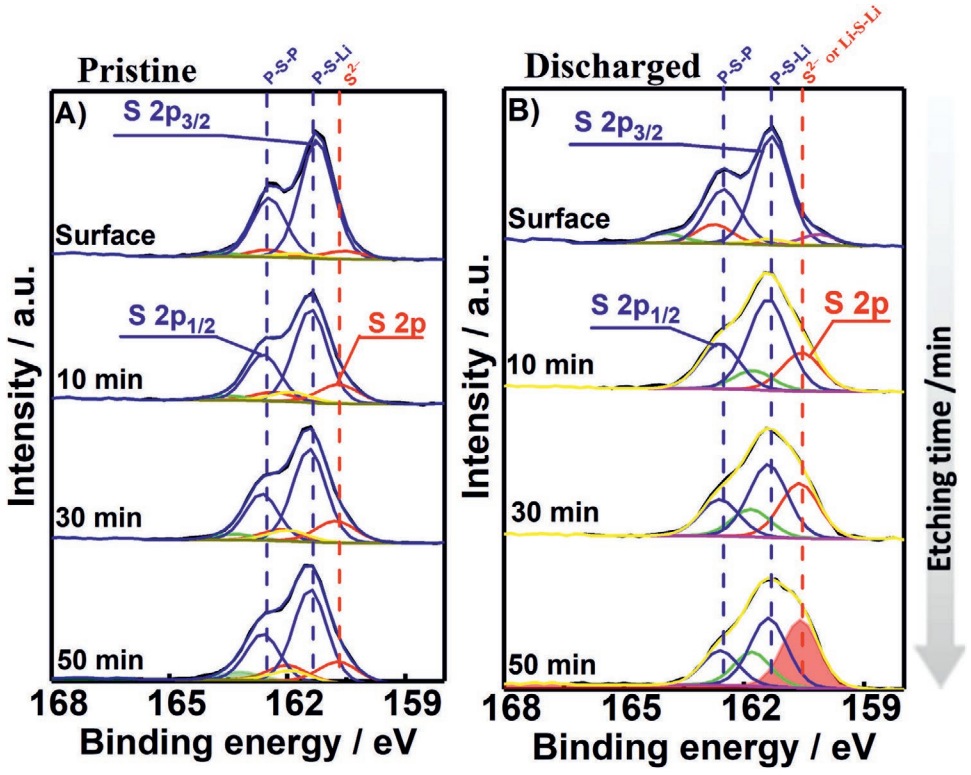

Figure 5. X-ray photoelectron spectroscopy (XPS) spectra and curve fitting results for A) the pristine cathode and B) the cathode after discharging to 0.7 V (0.1 C).

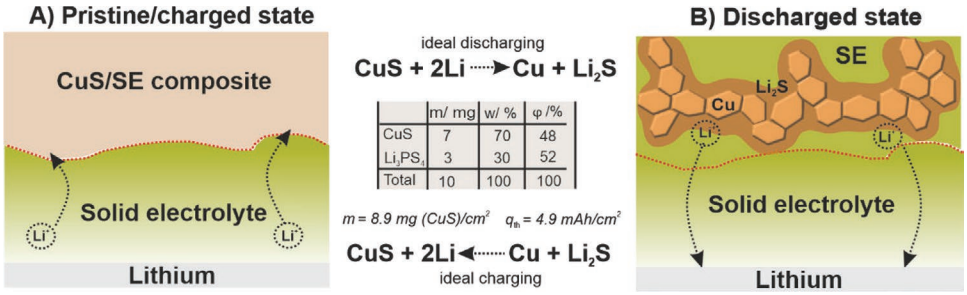

Figure 6. Schematic representation of the CuS solid-state lithium battery reacting according to Equation (1). A) Pristine state B) discharged state. The table shows the specifications of the CuS composite electrode (absolute materials amounts for the electrode with a diameter of 10 mm, weight and volume fractions assuming bulk densities, areal loading of CuS, and theoretical areal specific capacity based on q_{th}(CuS) = 560 mAh g^{-1}. Practically achieved values for the specific capacity over cycling range from about 300 to 500 mAh g^{-1} (Figure 2).

were analyzed as described by Randau et al.[1b] **Figure 7** shows the specific energy and specific power based on the cell mass. The cell delivers a specific energy of 49 Wh kg^{-1} at a specific power of 10 W kg^{-1}. The obtained results are very competitive with previously reported solid-state cells with transition metal sulfides. The presented CuS cell performance also compares favorably with the corresponding NMC cell of almost identical cell design by Randau et al.[1b] However, it is to be noted when interpreting this data that these cells have not been optimized in terms of all cell parameters and rather demonstrate fundamental investigations into new cell chemistries. However, the recently published NMC cell by Lee et al. with overall optimized separator, electrodes and cell design demonstrate the true potential of SSBs, several principles of which should also be applicable to cells using transition metal sulfides. In comparison with other cathode active materials, we believe that the good performance of CuS is due to its unique properties, combining high ductility, high electronic and ionic conductivity and specific structural features that enables a displacement reaction even in SSBs at room temperature and without the addition of carbon as conductive additive.

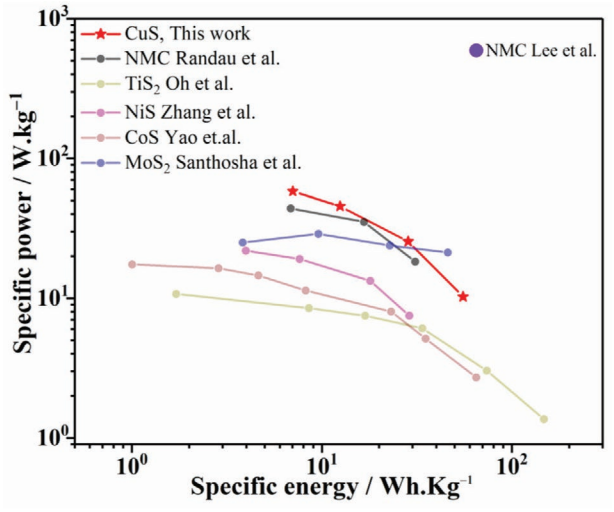

Figure 7. Ragone plot of the ambient temperature performance of solid-state batteries with transition metal sulfides CoS,[7] TiS_2,[6] NiS,[10] MoS_2,[9] NMC,[1b,33] and CuS (this work) as cathode, lithium as counter electrode, and thiophosphates as solid electrolyte. The performance of the SSBs is estimated from the current density, average charge–discharge voltage, and cell mass excluding current collectors and casing (i.e., only materials basis).

3. Conclusion

The use of CuS as cathode active material in Li-SSBs has been studied using the cell configuration Li|Li_3PS_4|[CuS 70 wt% + Li_3PS_4 (30 wt%)]. By combining the results from galvanostatic cycling, SEM, EDX, and XPS, we find that CuS undergoes a displacement reaction with lithium, leading to macroscopic phase separation of Cu and Li_2S. Cu crystallizes in micrometer-sized crystals that apparently form a continuous network throughout the cathode composite. Copper metal is even visible by eye. The reaction is reversed upon charging with the ICE reaching 95%. The displacement mechanism is in line with findings for cells with liquid electrolyte although the Cu crystals seem to grow much larger in the solid-state cell. The observation of a displacement reaction in the solid-state configuration is surprising given the large volume expansion. Moreover, excellent cycle life is found reaching 310 mAh g^{-1} after 100 cycles. Even upon prolonged cycling, the voltage profiles confirm a two-step reaction mechanism meaning that an intermediate phase forms. A comparison with literature in a Ragone plot shows that the cells are among the best conversion-type SSBs reported so far.

Overall, this study demonstrates that displacement reactions in the solid-state may be efficient and reversible enough to be used in rechargeable batteries at room temperature. The use of CuS and the solid-state approach mitigates two major limitations of conversion reactions that are large polarization and often low ICE values. The findings are likely due to the beneficial combination of several materials properties, i.e., ductility of the active material and the SE, reasonable stability within the electrochemical stability window of the electrolyte, the displacement mechanism as well as the intrinsic mixed conductivity of copper sulfides.

4. Experimental Section

Synthesis of CuS by Solid-State Method: CuS was prepared by solid-state reaction from high purity Copper (Sigma Aldrich, 99.9%) and

Sulphur (Sigma Aldrich, 99.9%). Stoichiometric amounts of of Cu and S were grinded in an agate mortar for about 15 min and the powder was then ball milled (Pulverisette 7 Premium line, Fritsch) in a ZrO_2 jar (80 mL) at 300 rpm for 3 h using ZrO_2 balls (d = 10 mm, 10 number) with a volumetric ball to powder ratio of 1:10. The obtained powder was heated at 100 °C, 200 °C, and 300 °C in vacuum for about 3 h to get high crystalline CuS, which were used to prepare the electrodes. All sample handling was done in an Ar filled glove box to avoid side reactions.

Instrumentation and Structural Characterization: PXRD measurements were conducted using Bruker D2 discover diffractometer with Cu Kα (λ = 1.5406 Å), angular range of $10° < 2\theta < 80°$ in a step size of 0.02° and scan rate 1 s step^{-1}. The experimental diffraction patterns were compared with slandered JCPDS file number 06-0464 of CuS hexagonal covellite phase. The microstructure images of the CuS is obtained by SEM, 5 µL of CuS in ethanol suspension is drop casted on to silicon substrate and dried overnight at room temperature (25 °C). The samples are investigated by high-resolution field emission (FE) SEM (Carl-Zeiss AG, Germany). Top-view microstructure images of dissembled cells were obtained from the cathode side of pristine and one discharged solid-state cell. TGA measurements were conducted using the Netzsch STA 449 F3 Jupiter with a heating rate of 10 °C min^{-1} and oxygen gas flow rate is 50 mL min^{-1}.

XPS measurements were carried out using a PHI5000 Versa probe II (Physical Electronics GmbH) with an Al anode. To avoid air exposure, the sample pellets were transferred from an argon filled glovebox to the analysis chamber using a transfer vessel filled with an argon gas. Reaction products of the composite cathode were quantified as a function of depth at the cathode composite and SE interface on the cathode side. Secondary electron imaging (SXI) was used in order to select an analysis area that was representative of the sample surface morphology. The probed surface area was 200 × 1400 µm and an X-ray power of 100 W was used. Depth profiling was performed by switching between monochromatic Al Kα X-rays for surface analysis and Ar^+ ions for sputtering. The pass energy of the analyzer was set to 23.5 eV for detailed spectra. All the measurements were evaluated using the CasaXPS software.

Assembly of Solid-State Cell and Electrochemical Measurements: SSBs were constructed in the following materials sequence: Li|Li_3PS_4|[CuS 70 wt% + Li_3PS_4 (30 wt%)]. The composite cathode was prepared by gently mixing the CuS and SE in the weight ratio of 70:30 (volume ratio is 48:52) in agate mortar for about 15 min. For the cell construction, 70 mg of SE was placed in the 10 mm die and cold pressed at 3 tons for 3 min and subsequently 10 mg of composite cathode was pressed at 3 tons for 3 min on top of the SE to form the bilayer pellet of ≈470 µm thickness. The counter electrode, lithium (Rockwood Lithium, 99.8%, 120 µm thickness, d = 10 mm) were connected on the other side of the bilayer pellet and sandwiched by the two stainless steel pistons which act as current collectors. During electrochemical measurements, a constant reduced weight of approximately 50 kg was applied. All the composite preparation and cell construction was performed inside an argon-filled glove box (H_2O and O_2 levels below 1 ppm, MBraun, Germany)

The electrochemical measurements were conducted with the above-mentioned solid-state cell by using the Bio-logic MPG2 multichannel cycler. The galvanostatic charge–discharge was conducted in the voltage range from 0.7 to 3.0 V versus Li^+/Li at a constant current of 0.1 C (560 mA g^{-1}) for long-term cycling. For rate capability testing, different current density of 0.1, 0.5, 0.2, and 1 C for 5 cycles at each rate and then switching back to the cycling at a low current density of 0.1 C. All measurements were carried at room temperature (22 °C).

Supporting Information

Supporting Information is available from the Wiley Online Library or from the author.

Acknowledgements

The authors thank the Federal Ministry for Education and Research (BMBF) for financial support within the projects FELIZIA and NASEBER (grant numbers: 03XP0026I, 03XP0026J, 03XP0187D, and 03XP0187C).

Open access funding enabled and organized by Projekt DEAL.

Conflict of Interest

The authors declare no conflict of interest.

Keywords

CuS, displacement conversion reactions, high energy density, solid-state batteries, sulfide solid electrolytes

Received: July 24, 2020
Revised: August 28, 2020
Published online: September 28, 2020

[1] a) Y. Kato, S. Hori, T. Saito, K. Suzuki, M. Hirayama, A. Mitsui, M. Yonemura, H. Iba, R. Kanno, *Nat. Energy* **2016**, *1*, 16030; b) S. Randau, D. A. Weber, O. Kötz, R. Koerver, P. Braun, A. Weber, E. Ivers-Tiffée, T. Adermann, J. Kulisch, W. G. Zeier, F. H. Richter, J. Janek, *Nat. Energy* **2020**, *5*, 259; c) A. Manthiram, X. Yu, S. Wang, *Nat. Rev. Mater.* **2017**, *2*; d) K. Xu, *ACS Chem. Rev.* **2004**, *104*, 4303; e) Y.-S. Hu, *Nat. Energy* **2016**, *1*, 16042; f) T. Famprikis, P. Canepa, J. A. Dawson, M. S. Islam, C. Masquelier, *Nat. Mater.* **2019**, *18*, 1278.

[2] a) J. Mindemark, M. J. Lacey, T. Bowden, D. Brandell, *Prog. Polym. Sci.* **2018**, *81*, 114; b) Z. Xue, D. He, X. Xie, *J. Mater. Chem. A* **2015**, *3*, 19218.

[3] a) R. Chen, Q. Li, X. Yu, L. Chen, H. Li, *Chem. Rev.* **2020**, *120*, 6820; b) D. H. S. Tan, A. Banerjee, Z. Chen, Y. S. Meng, *Nat. Nanotechnol.* **2020**, *15*, 170; c) F. Wu, J. Maier, Y. Yu, *Chem. Soc. Rev.* **2020**, *49*, 1569.

[4] a) N. Kamaya, K. Homma, Y. Yamakawa, M. Hirayama, R. Kanno, M. Yonemura, T. Kamiyama, Y. Kato, S. Hama, K. Kawamoto, A. Mitsui, *Nat. Mater.* **2011**, *10*, 682; b) J. Lau, R. H. DeBlock, D. M. Butts, D. S. Ashby, C. S. Choi, B. S. Dunn, *Adv. Energy Mater.* **2018**, *8*, 1800933; c) Z. Zhang, Y. Shao, B. Lotsch, Y.-S. Hu, H. Li, J. ü r. Janek, L. F. Nazar, C.-W. Nan, J. Maier, M. Armand, L. Chen, *Energy Environ. Sci.* **2018**, *11*, 1945; d) Y. Xiao, Y. Wang, S.-H. Bo, J. C. Kim, L. J. Miara, G. Ceder, *Nat. Rev. Mater.* **2020**, *5*, 105.

[5] A. L. Santhosha, L. Medenbach, J. R. Buchheim, P. Adelhelm, *Batteries Supercaps* **2019**, *2*, 524.

[6] D. Y. Oh, Y. E. Choi, D. H. Kim, Y.-G. Lee, B.-S. Kim, J. Park, H. Sohnd, Y. S. Jung, *J. Mater. Chem. A* **2016**, *4*, 10329.

[7] X. Yao, D. Liu, C. Wang, P. Long, G. Peng, Y. S. Hu, H. Li, L. Chen, X. Xu, *Nano Lett.* **2016**, *16*, 7148.

[8] J. M. Whiteley, S. Hafner, S. S. Han, S. C. Kim, K. H. Oh, S.-H. Lee, *Adv. Energy Mater.* **2016**, *6*, 1600495.

[9] A. L. Santhosha, P. K. Nayak, K. Pollok, F. Langenhorst, P. Adelhelm, *J. Phys. Chem. C* **2019**, *123*, 12126.

[10] Q. Zhang, G. Peng, J. P. Mwizerwa, H. Wan, L. Cai, X. Xu, X. Yao, *J. Mater. Chem. A* **2018**, *6*, 12098.

[11] S. Wenzel, D. A. Weber, T. Leichtweiss, M. R. Busche, J. Sann, J. Janek, *Solid State Ionics* **2016**, *286*, 24.

[12] a) R. Koerver, W. Zhang, L. de Biasi, S. Schweidler, A. O. Kondrakov, S. Kolling, T. Brezesinski, P. Hartmann, W. G. Zeier, J. Janek, *Energy*

Environ. Sci. **2018**, *11*, 2142; b) A. Sakuda, N. Nakamoto, H. Kitaura, A. Hayashi, K. Tadanaga, M. Tatsumisago, *J. Mater. Chem.* **2012**, *22*, 15247.

[13] J. M. Doux, H. Nguyen, D. H. S. Tan, A. Banerjee, X. Wang, E. A. Wu, C. Jo, H. Yang, Y. S. Meng, *Adv. Energy Mater.* **2019**, *10*, 1903253.

[14] D. J. Chakrabarti, D. E. Laughlin, *Bull. Alloy Phase Diagrams* **1983**, *4*, 254.

[15] a) J. Cabana, L. Monconduit, D. Larcher, M. R. Palacin, *Adv. Mater.* **2010**, *22*, E170; b) S. H. Yu, X. Feng, N. Zhang, J. Seok, H. D. Abruna, *Acc. Chem. Res.* **2018**, *51*, 273; c) Y. Lu, L. Yu, X. W. Lou, *Chem* **2018**, *4*, 972.

[16] Q. Su, L. Yao, J. Zhang, G. Du, B. Xu, *ACS Appl. Mater. Interfaces* **2015**, *7*, 23062.

[17] F. Klein, B. Jache, A. Bhide, P. Adelhelm, *Phys. Chem. Chem. Phys.* **2013**, *15*, 15876.

[18] a) F. Klein, R. Pinedo, P. Hering, A. Polity, J. Janek, P. Adelhelm, *J. Phys. Chem. C* **2016**, *120*, 1400; b) F. Klein, R. Pinedo, B. B. Berkes, J. Janek, P. Adelhelm, *J. Phys. Chem. C* **2017**, *121*, 8679.

[19] A. Débart, L. Dupont, R. Patrice, J. M. Tarascon, *Solid State Sci.* **2006**, *8*, 640.

[20] B. Jache, B. Mogwitz, F. Klein, P. Adelhelm, *J. Power Sources* **2014**, *247*, 703.

[21] a) A. Hayashi, T. Ohtomo, F. Mizuno, K. Tadanaga, M. Tatsumisago, *Electrochem. Commun.* **2003**, *5*, 701; b) A. Hayashi, T. Ohtomo, F. Mizuno, K. Tadanaga, M. Tatsumisago, *Electrochim. Acta* **2004**, *50*, 893; c) N. Machida, K. Kobayashi, Y. Nishikawa, T. Shigematsua, *Solid State Ionics* **2004**, *175*, 247; d) A. Hayashi, R. Ohtsubo, T. Ohtomo, F. Mizuno, M. Tatsumisago, *J. Power Sources* **2008**, *183*, 422; e) A. Hayashi, R. Ohtsubo, M. Tatsumisago, M. Nagao, *J. Mater. Sci.* **2010**, *45*, 377.

[22] W. Schumann, *Minerals of the World*, 2nd ed., Sterling **2000**.

[23] K. Okamoto, S. Kawai, *Jpn. J. Appl. Phys.* **1973**, *12*, 1130.

[24] a) G. Kalimuldina, I. Taniguchi, *J. Mater. Chem. A* **2017**, *5*, 6937; b) K. He, Z. Yao, S. Hwang, N. Li, K. Sun, H. Gan, Y. Du, H. Zhang, C. Wolverton, D. Su, *Nano Lett.* **2017**, *17*, 5726; c) J. S. Nam, J.-H. Lee, S. M. Hwang, Y.-J. Kim, *J. Mater. Chem. A* **2019**, *7*, 11699.

[25] C. Wu, S.-H. Yu, S. Chen, G. Liu, B. Liu, *J. Mater. Chem.* **2006**, *16*, 3326.

[26] J. Kasnatscheew, M. Evertz, B. Streipert, R. Wagner, R. Klopsch, B. Vortmann, H. Hahn, S. Nowak, M. Amereller, A. C. Gentschev, P. Lamp, M. Winter, *Phys. Chem. Chem. Phys.* **2016**, *18*, 3956.

[27] a) K. Jiang, Z. Chen, X. Meng, *ChemElectroChem* **2019**, *6*, 2825; b) F. Han, W.-C. Li, D. Li, A.-H. Lu, *ChemElectroChem* **2014**, *1*, 733; c) L. Duchêne, R. S. Kühnel, E. Stilp, E. Cuervo Reyes, A. Remhof, H. Hagemann, C. Battaglia, *Energy Environ. Sci.* **2017**, *10*, 2609.

[28] S. M. Hosseini, A. Varzi, S. Ito, Y. Aihara, S. Passeri, *Energy Storage Mater.* **2020**, *27*, 61.

[29] a) T. Swamy, X. Chen, Y.-M. Chiang, *Chem. Mater.* **2019**, *31*, 707; b) T. Hakari, M. Nagao, A. Hayashi, M. Tatsumisago, *J. Power Sources* **2015**, *293*, 721; c) T. Hakari, M. Deguchi, K. Mitsuhara, T. Ohta, K. Saito, Y. Orikasa, Y. Uchimoto, Y. Kowada, A. Hayashi, M. Tatsumisago, *Chem. Mater.* **2017**, *29*, 4768.

[30] a) J. Vetter, P. Novák, M. R. Wagner, C. Veit, K. C. Möller, J. O. Besenhard, M. Winter, M. Wohlfahrt-Mehrens, C. Vogler, A. Hammouche, *J. Power Sources* **2005**, *147*, 269; b) J. Ma, B. Chen, L. Wang, G. Cui, *J. Power Sources* **2018**, *392*, 94; c) K. Kerman, A. Luntz, V. Viswanathan, Y.-M. Chiang, Z. Chen, *J. Electrochem. Soc.* **2017**, *164*, A1731.

[31] a) K. N. Wood, K. X. Steirer, S. E. Hafner, C. Ban, S. Santhanagopalan, S. H. Lee, G. Teeter, *Nat. Commun.* **2018**, *9*, 2490; b) S. Wenzel, S. Randau, T. Leichtweiß, D. A. Weber, J. Sann, W. G. Zeier, J. Janek, *Chem. Mater.* **2016**, *28*, 2400.

[32] S. Ohno, R. Koerver, G. Dewald, C. Rosenbach, P. Titscher, D. Steckermeier, A. Kwade, J. Janek, W. G. Zeier, *Chem. Mater.* **2019**, *31*, 2930.

[33] Y.-G. Lee, S. Fujiki, C. Jung, N. Suzuki, N. Yashiro, R. Omoda, D.-S. Ko, T. Shiratsuchi, T. Sugimoto, S. Ryu, J. H. Ku, T. Watanabe, Y. Park, Y. Aihara, D. Im, I. T. Han, *Nat. Energy* **2020**, *5*, 299.